

## Surface warming in global cities is substantially more rapid than in rural background areas

Zihan Liu<sup>1</sup>, Wenfeng Zhan<sup>1,2✉</sup>, Benjamin Bechtel<sup>3</sup>, James Voogt<sup>4</sup>, Jiameng Lai<sup>1</sup>, Tirthankar Chakraborty<sup>5,6</sup>, Zhi-Hua Wang<sup>7</sup>, Manchun Li<sup>1✉</sup>, Fan Huang<sup>1</sup> & Xuhui Lee<sup>5✉</sup>

Warming trends in cities are influenced both by large-scale climate processes and by local-scale urbanization. However, little is known about how surface warming trends of global cities differ from those characterized by weather observations in the rural background. Here, through statistical analyses of satellite land surface temperatures (2002 to 2021), we find that the mean surface warming trend is  $0.50 \pm 0.20$  K·decade<sup>-1</sup> (mean  $\pm$  one S.D.) in the urban core of 2000-plus city clusters worldwide, and is 29% greater than the trend for the rural background. On average, background climate change is the largest contributor explaining  $0.30 \pm 0.11$  K·decade<sup>-1</sup> of the urban surface warming. In city clusters in China and India, however, more than  $0.23$  K·decade<sup>-1</sup> of the mean trend is attributed to urban expansion. We also find evidence of urban greening in European cities, which offsets  $0.13 \pm 0.034$  K·decade<sup>-1</sup> of background surface warming.

<sup>1</sup>Jiangsu Provincial Key Laboratory of Geographic Information Science and Technology, International Institute for Earth System Science, Nanjing University, Nanjing, Jiangsu 210023, China. <sup>2</sup>Jiangsu Center for Collaborative Innovation in Geographical Information Resource Development and Application, Nanjing 210023, China. <sup>3</sup>Department of Geography, Ruhr-University Bochum, 44801 Bochum, Germany. <sup>4</sup>Department of Geography, Western University, London, ON N6A 5C2, Canada. <sup>5</sup>School of Forestry and Environmental Studies, Yale University, New Haven, CT 06511, USA. <sup>6</sup>Atmospheric Sciences and Global Change Division, Pacific Northwest National Laboratory, Richland, WA 99354, USA. <sup>7</sup>School of Sustainable Engineering and the Built Environment, Arizona State University, Tempe, AZ 85287, USA. ✉email: [zhanwenfeng@nju.edu.cn](mailto:zhanwenfeng@nju.edu.cn); [limanchun@nju.edu.cn](mailto:limanchun@nju.edu.cn); [Xuhui.lee@yale.edu](mailto:Xuhui.lee@yale.edu)

Urban residents can experience greater heat exposure during heatwave events than the general population because of the urban heat island (UHI)<sup>1,2</sup>, the phenomenon of higher temperatures over urban land than over the surrounding rural land<sup>3</sup>. This problem will become more severe in the future because of global climate change and urban population growth in cities<sup>4,5</sup>. Despite the prevalence of the UHI and the increasing recognition of the need for climate monitoring in urban environments<sup>3</sup>, a great majority of the assessments of heat-related mortality<sup>6</sup> and loss of workplace productivity<sup>7</sup> in cities are still based on temperature data collected by non-urban and peri-urban weather stations<sup>8</sup>. Furthermore, although the urban effect has been considered in projections of heat exposure in the future<sup>9</sup>, many studies make an implicit assumption that urban temperatures will increase at an equal-rate as rural temperatures<sup>6,10</sup>.

Some studies have examined the equal-rate assumption by isolating the urban warming signal from surface air temperature (SAT) data, i.e., by directly separating contributions of urbanization from other forcing factors based on linear or non-linear models<sup>11,12</sup>. This approach has been applied to China where rapid urbanization has occurred in the past decades and where the density of weather station network is high<sup>13</sup>. It is estimated that urbanization-induced warming accounts for 20% to 50% of the overall observed warming in areas that have experienced fast urbanization<sup>13,14</sup>. However, these studies focused more on urbanization contribution to regional warming rather than on warming within cities. Urban stations used in previous urban warming studies were mostly located in urban fringes (i.e., newly urbanized areas) rather than located in urban cores. This is primarily because most of these urban stations were initially installed over rural surfaces, while they became 'true' urban ones when they are gradually engulfed by built-up areas due to rapid urbanization, especially in developing countries such as China<sup>14–16</sup>. For example, a previous investigation of urban warming in China indicates stations that suffered from inhomogeneities (e.g., changes in observation instrument, site, and time, as well as the urbanization effect) account for about a half of the total stations<sup>14</sup>. The inhomogeneities in SAT series could directly affect urban–rural differences in SAT trend and thus bias the estimation of urban warming trend<sup>14,16</sup>. Furthermore, previous reports of urban warming derived from urban–rural temperature differences typically represent the characteristics of the stations located at a local scale<sup>16</sup>. It is not known if the results of these studies can be extended to other geographic regions.

Other studies have examined the urban warming signal by comparing temperature observations in urban areas with those observed in rural surroundings or those retrieved from reanalysis data<sup>17,18</sup>. A non-zero UHI intensity trend would indicate that urban and rural temperatures are changing at different rates. The SAT-based UHI intensity trends have been reported for individual cities and city clusters in single regions<sup>19,20</sup> and for selected cities across different regions of the world<sup>21,22</sup>. The largest SAT-based nighttime UHI trends of around 0.40 K decade<sup>-1</sup> have been observed for megacities such as London, Osaka, and Shanghai<sup>22</sup>. One concern here is that limited urban stations are difficult to provide sufficient spatial details for complex urban neighborhoods<sup>14,23</sup>. Another complication is that in-situ paired observations of SAT are unavailable for the majority of global cities. Satellite LST can overcome these difficulties to some degree. Studies indicate that the global mean LST-based UHI trends are positive (0.29 ± 0.41 K decade<sup>-1</sup>) during the day and relatively small (0.10 ± 0.23 K decade<sup>-1</sup>)<sup>24</sup> or near zero (0.00 ± 0.010 K decade<sup>-1</sup>) at night<sup>25</sup>. However, these LST-based studies have not separated the warming signal of the urban core from the change signal resulting from conversion of pixels from rural to urban

during the study period, which is likely to cause overestimation of the true warming trends of global cities.

Here, we investigate the urban surface warming trends with satellite LST data collected over 2000-plus city clusters worldwide and compare them with the trends observed in rural land parcels. We divide the pixels in each cluster and its adjacent buffer into three categories: (1) urban core, where land use remains urban throughout the detection period (2002 to 2021), (2) rural background, where land use remains rural, and (3) transitional land, where the land use was initially rural and became urban during the study period. Our focus is the urban core temperature trends. A statistical attribution method is used to separate the trends into contributions from urban expansion (URB), background climate change (BCC), and landscape greening (LSG) within urban cores. We find that urban core temperatures increase at a faster rate than rural background temperatures. In spite of the different representation between LST and SAT (refer to Supplementary Note 1), our results highlight the necessity to consider the surface warming rate difference between urban core and rural background towards the assessments of heat-related morbidity and mortality as well as the projection of heat exposure in the future.

## Results

**Urban surface warming trends.** We observe faster surface warming trends at the urban core than in the adjacent rural area. The global mean surface warming trend within the urban core is 0.56 ± 0.21 K decade<sup>-1</sup> (mean ± one standard deviation) during the day and 0.43 ± 0.16 K decade<sup>-1</sup> at night (Fig. 1a, b; Supplementary Table 1). Both of these trends are statistically significant ( $p < 0.05$ ). For comparison, the surface warming trend at the rural pixels is 0.40 ± 0.23 K decade<sup>-1</sup> during the day and 0.37 ± 0.21 K decade<sup>-1</sup> at night ( $p < 0.05$ ) (Supplementary Fig. 1a, b). The daily mean surface warming trend (i.e., mean daily conditions averaged over daytime and nighttime) is 0.50 ± 0.20 K decade<sup>-1</sup> at the urban core, which is 29% greater than the trend for the rural background (0.38 ± 0.21 K decade<sup>-1</sup>). These two LST trends are both greater than the daily mean SAT trend (0.32 ± 0.083 K decade<sup>-1</sup>) ( $p < 0.05$ ) calculated with reanalysis SAT data for the same city clusters (Supplementary Fig. 2). We further observe that these trends calculated by annual mean LSTs are generally higher than the trends measured by mean LSTs of summer (Supplementary Table 1). The reason for the discrepancy could be related to a higher EVI trend in summer (Supplementary Table 1).

The urban surface warming trend (i.e., warming trends at the urban core) varies among cities of different sizes and in different continents (Fig. 2). The surface warming trend generally increases with city size (Fig. 2a, b). During the day, the mean trend increases from 0.41 ± 0.25 K decade<sup>-1</sup> for small cities (area < 65 km<sup>2</sup>, total number 520; see Methods for city classification) to 0.69 ± 0.24 K decade<sup>-1</sup> for megacities (area > 450 km<sup>2</sup>, total number 520); at night, the trend increases from 0.37 ± 0.21 K decade<sup>-1</sup> for small cities to 0.50 ± 0.20 K decade<sup>-1</sup> for megacities. Nevertheless, it should be noted that such relations between surface warming trend and city sizes might be affected by regional surface warming patterns. For example, there are a considerable amount of large megacities distributed in Asia. By continent, the Asian urban surface warming trends are most pronounced, at a mean rate of 0.71 ± 0.34 K decade<sup>-1</sup> during the day and 0.53 ± 0.25 K decade<sup>-1</sup> at night (Fig. 2c, d). The lowest daytime trend occurs in Europe (0.44 ± 0.24 K decade<sup>-1</sup>) and the lowest nighttime trend occurs in Oceania (0.37 ± 0.11 K decade<sup>-1</sup>). We find that ratios of surface warming trend between urban core and rural background show a similar pattern with a surface warming trend over urban core (Supplementary Fig. 3). This is mostly

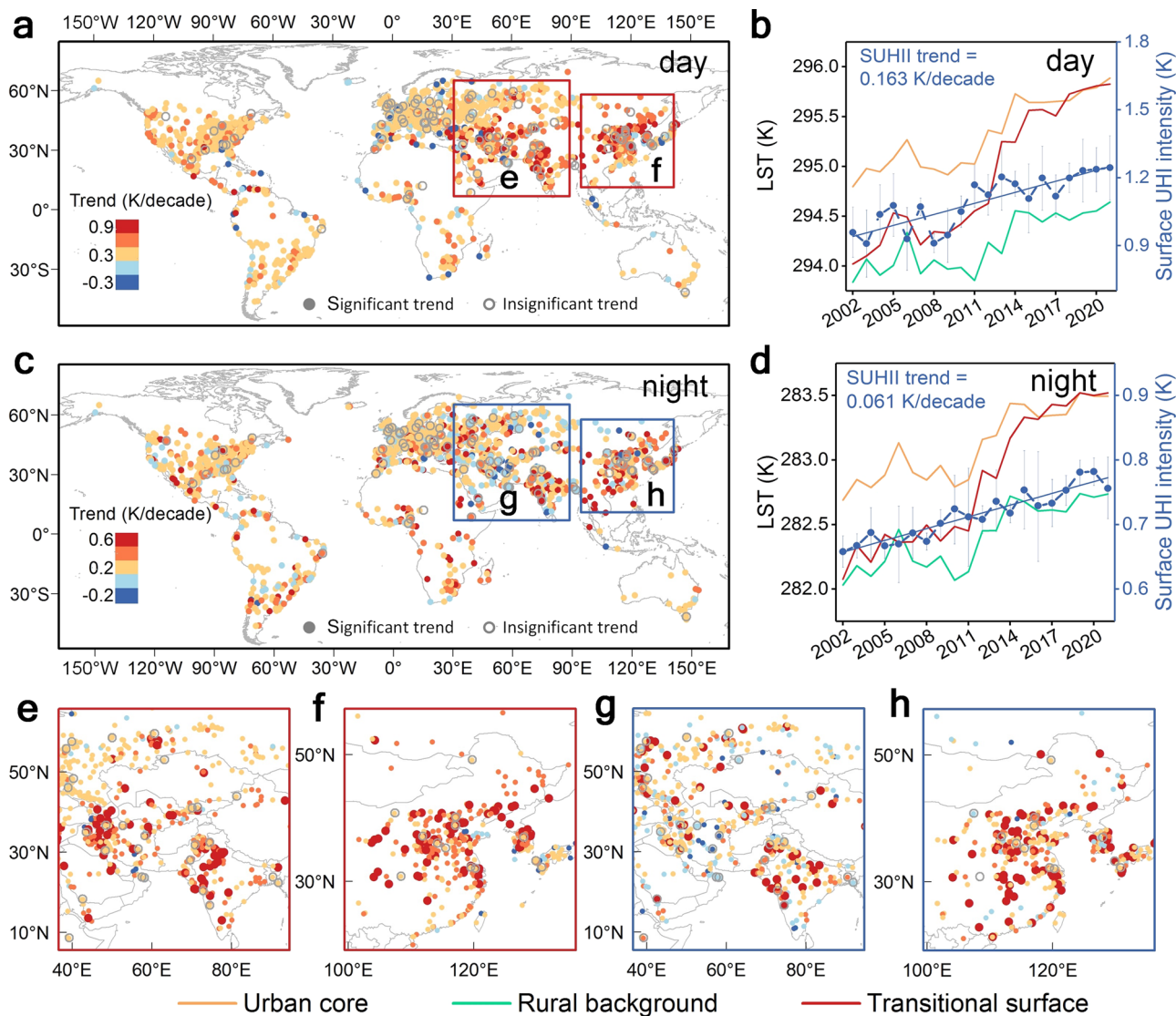


**Fig. 1** Surface warming trends at the urban core across the world. Map of daytime trend (a), map of nighttime trend (c), and global mean trend in daytime (b), and nighttime surface UHI intensity (d). The two boxed regions in a, c are enlarged as e, f for daytime and g, h for nighttime. Note that the error bars represent 10%-90% percentiles.

because there are small deviations in the surface warming trends over rural background for cities of different sizes and for cities across various continents (Supplementary Fig. 4).

Unsurprisingly, of the three land use types, the transitional land experiences the strongest surface warming, at an average rate of  $1.06 \pm 0.41 \text{ K decade}^{-1}$  during the day and  $0.84 \pm 0.39 \text{ K decade}^{-1}$  at night (Supplementary Fig. 1c, d). The main cause is the loss of evaporative cooling power from the conversion of the pixels from natural land to impervious surfaces (Supplementary Fig. 5). Building construction over the transitional land that is more biased towards either small or large low rise (e.g., warehouse type) buildings may also contribute to the larger daytime surface warming trend when viewed as LST<sup>26</sup>.

Both the urban core and rural land show increasing trends of vegetation greenness. The mean EVI (Enhanced Vegetation Index) trend is  $0.0039 \pm 0.0017 \text{ decade}^{-1}$  at the urban core ( $p < 0.05$ ) and  $0.0083 \pm 0.0026 \text{ decade}^{-1}$  at the rural land ( $p < 0.05$ ). The mean EVI trend at the rural land pixels is essentially the same as that reported for the global land surface obtained from the previous study by Zhang et al.<sup>27</sup>. The largest regional urban mean urban EVI trend occurs in Europe

( $0.012 \pm 0.0032 \text{ decade}^{-1}$ ), while decreasing trends occur in Africa ( $-0.0088 \pm 0.0031 \text{ decade}^{-1}$ ) and South America ( $-0.0091 \pm 0.0037 \text{ decade}^{-1}$ ; Supplementary Fig. 5). This regional pattern is similar to the pattern reported for urban vegetation cover<sup>28</sup> and it differs from the greening trend of forest landscapes where substantial greening has been observed in tropical forests in Africa, South America, and Southeast Asia<sup>29</sup>. The faster urban greening trend in Europe may be due to the combination of elevated urban warming, CO<sub>2</sub> fertilization, and expansion of green space<sup>29,30</sup>. Such an increase of urban greening trend is consistent with the observed advance in spring phenology over time across Europe<sup>31</sup>. On the other hand, the declining EVI trends in Africa and South America indicate reduction of green spaces in cities<sup>28</sup>. Positive greening trends in cities such as Beijing (Supplementary Fig. 5) may be attributable to the combination of urban warming and CO<sub>2</sub> fertilization<sup>29</sup> and expansion of green space<sup>32,33</sup>.

Substantial increasing trends of the daytime and nighttime satellite LST-derived surface UHI (SUHI) intensity are detected for 87% and 72% of the city clusters, respectively ( $p < 0.05$ ; Supplementary Fig. 6). A small portion (12%) of the clusters,

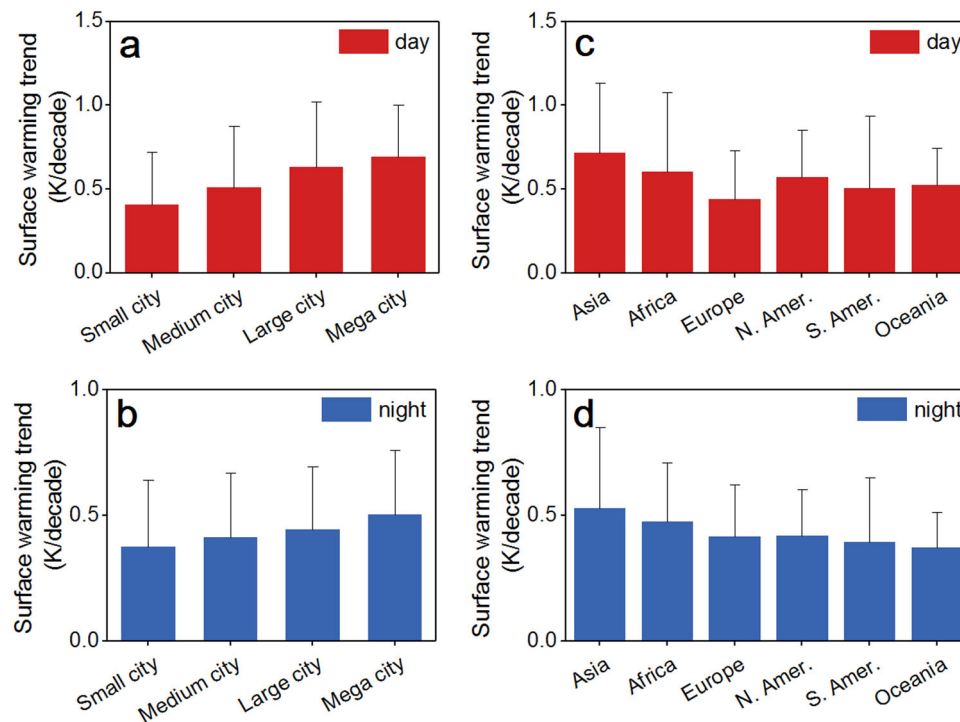


**Fig. 2** Surface warming trend at the urban core by city size and continent. Note that the error bars represent 10%-90% percentiles.

mostly located in northern Asia, has experienced a significant declining trend in the daytime SUHI ( $p < 0.05$ ). A larger portion (28%), mostly located in the Middle and Near East, shows significant declining trends in the nighttime SUHI ( $p < 0.05$ ). The global mean SUHI trend is  $0.16 \pm 0.093 \text{ K decade}^{-1}$  during the day and  $0.060 \pm 0.033 \text{ K decade}^{-1}$  at night (Supplementary Table 1 and Supplementary Fig. 6). These global mean trends are much higher than those trends obtained from the previous study by Chakraborty and Lee<sup>25</sup> ( $0.030 \pm 0.020$  and  $0.00 \pm 0.01 \text{ K decade}^{-1}$  for the day and night, respectively), but are much lower than those trends obtained from previous study by Yao et al.<sup>24</sup> ( $0.29 \pm 0.41$  and  $0.10 \pm 0.23 \text{ K decade}^{-1}$  for the day and night, respectively) for global cities. These two studies have used the same satellite LST data but they differ from our study in how the transitional land is handled. The gradual incorporation of transitional land year by year in the previous study by Chakraborty and Lee<sup>25</sup> may have caused underestimation of the SUHI trend, because the temperature is usually lower in transitional land than in urban core. On the other hand, in the previous study by Yao et al.<sup>24</sup> the urban land remains constant during the study period and includes the urban core and all the transitional pixels; this approach may overestimate the SUHI trend due to the high surface warming trend of transitional land (Supplementary Table 1). Additionally, the sample sizes for the three studies also differ, with Chakraborty and Lee<sup>24</sup> considering the most number of cities and Yao et al.<sup>25</sup> considering the lowest cities, which would impact bulk trends. Regardless of the sample size and how the SUHI is calculated, these two studies and the present investigation all show the stronger SUHI trend during the daytime than nighttime.

**Attribution of urban surface warming.** On average, the contributions from BCC and URB to the daytime urban surface warming trend are  $0.34 \pm 0.13 \text{ K decade}^{-1}$  and  $0.27 \pm 0.13 \text{ K decade}^{-1}$ , respectively (Fig. 3a and Supplementary Table 2). About the same magnitude contributions of BCC ( $0.25 \pm 0.078 \text{ K decade}^{-1}$ ) and URB ( $0.21 \pm 0.094 \text{ K decade}^{-1}$ ) are also

observed at night (Fig. 3a). In addition to increasing the magnitudes of urban surface warming (Fig. 2) and SUHI intensity (Supplementary Fig. 7), increasing city size amplifies the URB contribution (Fig. 3b). The mean URB contribution increases from  $0.19 \pm 0.11 \text{ K decade}^{-1}$  for small cities (the corresponding mean areas is  $63 \text{ km}^2$ ) to  $0.28 \pm 0.13 \text{ K decade}^{-1}$  for megacities (the corresponding mean areas is  $475 \text{ km}^2$ ) (Supplementary Table 2). The Europe, North America, and Oceania continents display similar percent contributions by city size (Fig. 3c and Supplementary Table 3). Among the 2000+ city clusters, 90% have BCC as the greatest contributor to the urban core surface warming trend; these clusters are found in all the continents. A smaller percent (5%), located mainly in rapidly urbanizing regions in eastern China and in central and northern India, have URB as the greatest contributor to the surface warming trend (Fig. 4, Supplementary Figs. 8 and 9).

The global mean LSG contribution to the urban surface warming trend is lower in magnitude (it has an opposite sign) than the mean BCC and URB contributions. The magnitude contribution from LSG is  $-0.10 \pm 0.028 \text{ K decade}^{-1}$  for the day and  $-0.052 \pm 0.014 \text{ K decade}^{-1}$  at night (Fig. 3a). In other words, urban greening creates a cooling effect for both daytime and nighttime. In natural landscapes, replacement of bare land by vegetation (especially trees) generally warms the near-surface air at night<sup>30,34</sup> due to (1) reduced radiative cooling of the ground surface that results from sky view factor obstruction from tree canopy and (2) enhanced turbulence that brings warm air from above to the surface in stably-stratified conditions<sup>34</sup>. Here in the urban environment, the effect of vegetation is cooling at night, and the underlying mechanism may be related to reduction in daytime urban heat storage that leads to lower nighttime temperature<sup>35</sup>. The role of LSG seems to decrease with increasing urban size (Fig. 3b and Supplementary Fig. 10). Across continents, the most negative LSG contribution is observed for cities in Europe ( $-0.17 \pm 0.044 \text{ K decade}^{-1}$  and  $-0.10 \pm 0.025$  for the day and at night, respectively) where urban cores have experienced the highest rates of greening (Supplementary Fig. 5).

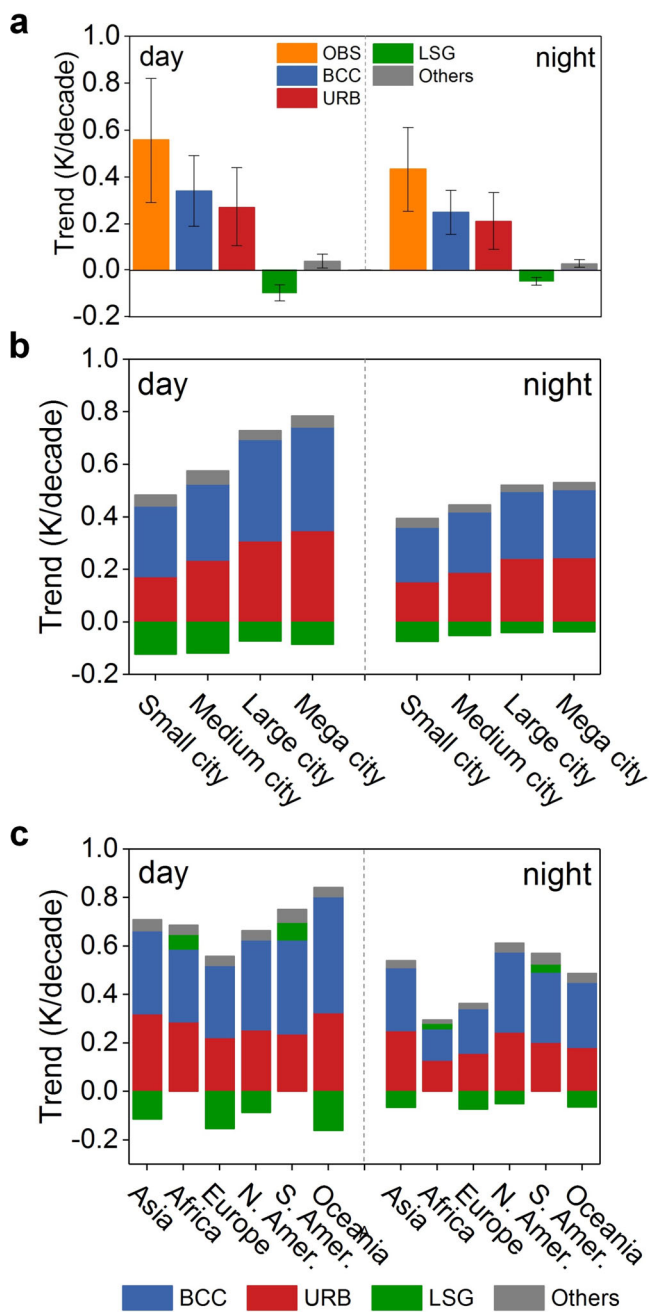


**Fig. 3 Contributions of background climate change (BCC), urbanization (URB), and landscape greening (LSG) to observed urban surface warming trends (OBS).** Mean contributions across the globe (a), mean contributions by city size (b), and mean contributions by continent (c). Error bars are  $\pm 1$  S.D. Note that “Others” represents the residual component that cannot be explained by these three selected parameters. Note that the error bars represent 10%–90% percentiles.

On the other hand, the LSG contribution is positive for Africa and South America ( $0.047 \pm 0.018$  K decade<sup>-1</sup> to  $0.064 \pm 0.035$  K decade<sup>-1</sup>), a result of gradual loss of vegetation in the urban cores (Supplementary Fig. 5)<sup>28</sup>. Interestingly, several cities in rapidly urbanizing areas in China experienced large negative LSG contribution (Fig. 4), possibly because of the substantial increase of vegetation cover induced by urban renewal in these cities<sup>33</sup>.

We further observe that the global mean LST trends are expected to increase by  $\sim 0.096$  K decade<sup>-1</sup> when population density increases by 100/km<sup>2</sup> per decade, while the trends would

decrease by around  $0.26$  K decade<sup>-1</sup> as EVI increases by 0.01 per decade (refer to Supplementary Note 2 and Table 4). These ratios between LST and population density (or EVI) trends differ largely among continents. The ratios between LST and population density trends are relatively smaller in Asia and Africa than in other continents, which may be attributable to the greater growth rates of population density in these two continents. There are relatively smaller ratios between LST and EVI trends in Europe, Africa, and South America, probably attributable to the relatively larger EVI trends in these three continents (Supplementary Table 4). These results may be helpful for providing a rough estimate of future urban surface warming due to both vegetation and population changes; and a link between these two (e.g., the counteraction of vegetation to urban population in surface warming) can potentially help design general guidelines for heat mitigation strategies.

### Implication

Previous urban warming studies have documented urbanization-induced regional warming by isolating the urban warming signal from in-situ SAT data or using satellite-derived LST but mostly without separating urban cores from transitional surfaces. In this study, we have divided urban pixels into urban core, rural background, and transitional areas. We demonstrate that the mean surface warming trend in the urban core of 2000-plus city clusters worldwide is 29% greater than the trend for the pixels in the rural background next to the urban land boundary. This percentage enhancement is even higher, at 56%, when referenced to the background temperature trend defined by atmospheric reanalysis data. This difference may result from the differences between satellite LST and reanalysis SAT. Another likely reason is that the rural pixels have been influenced by surface warming of urban core pixels and transitional pixels through advection and therefore are not true representation of background conditions. Such advective effect occurs at the urban–rural boundary, a spatial scale that is too small to be resolvable by the reanalysis modeling system. We acknowledge that satellite LST is not as accurate as SAT measured by weather stations because these two temperatures represent two different physical parameters (refer to Supplementary Note 1). However, here we concentrate not on absolute value but on trend, for which the LST–SAT difference should be substantially reduced. Although LST-based surface warming analysis do not serve as a surrogate for SAT-based investigation, it provides a different strategy that overcomes difficulties in finding proper urban–rural station SAT pairs particularly over global cities. More importantly, LST and SAT characterize distinct and complementary components of urban warming, and LST is still useful for various applications such as weather forecasting and prediction as it provides a lower boundary condition to the atmosphere. We admit possible uncertainties induced by the deficiencies of satellite LST and reanalysis SAT data, such as the data error, potential urbanization signals and natural oscillations of these two data sources<sup>11,36</sup>. Nevertheless, a closer analysis suggests such impacts should be minimal and may not induce a large bias on the major findings (refer to Supplementary Note 3).

It is well known that the surface UHI intensity generally increases with increasing city size<sup>37</sup>. Our results illustrate that the urban surface warming trend is also size-dependent. The largest surface warming trend,  $0.59 \pm 0.23$  K decade<sup>-1</sup>, or 47% greater than the trend of the rural background, is found for the group of 520 megacities. Currently, about 1.7 billion people live in these megacities with more than 1 million inhabitants. It is predicted that as urbanization continues, the number of megacities will increase, and so will the number of people who live in these

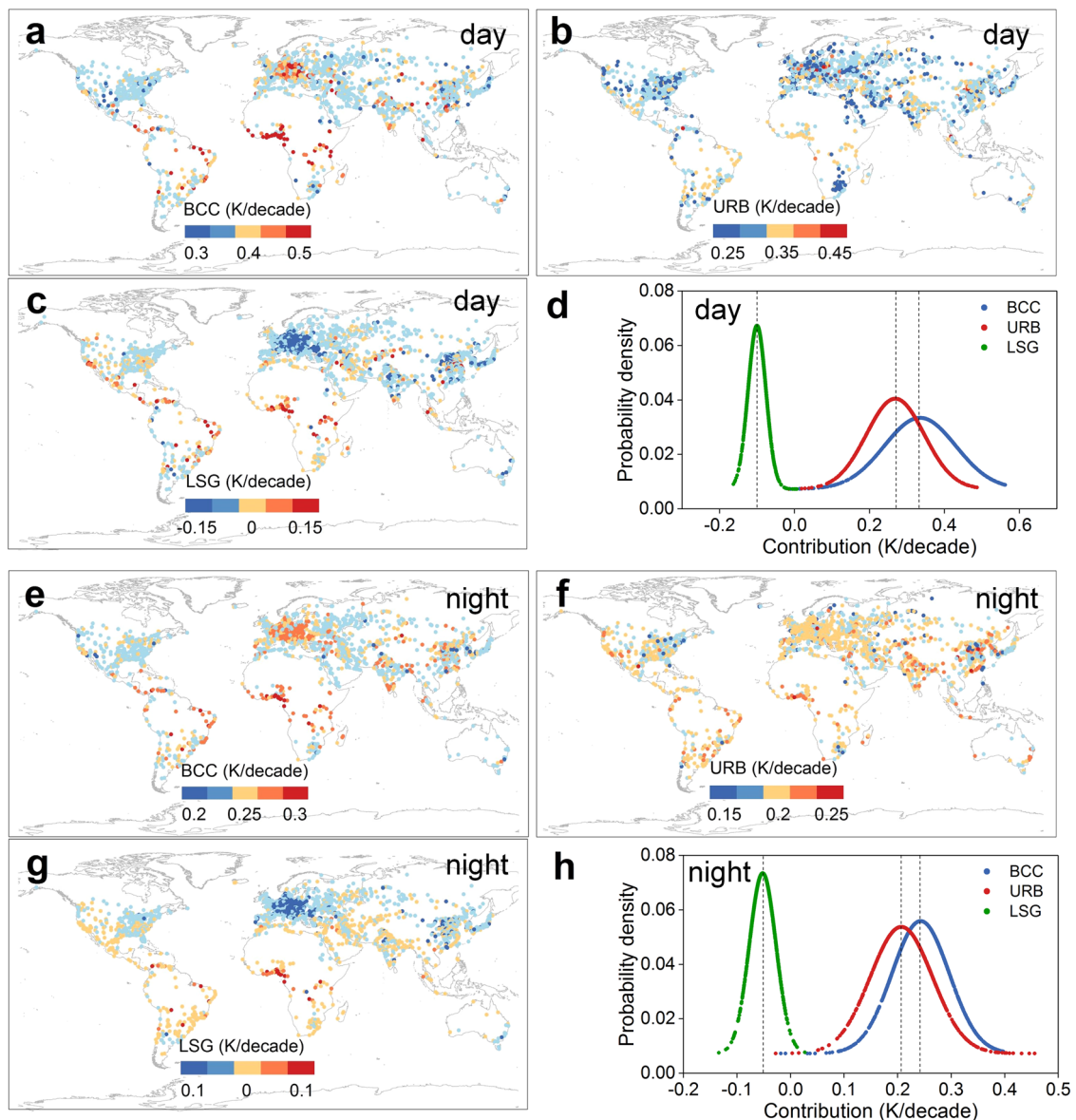


**Fig. 4** Separate contributions ( $\text{K decade}^{-1}$ ) of background climate change (BCC), urbanization (URB), and landscape greening (LSG) to urban surface warming trends. Map of daytime for BCC, URB, and LSG (a–c), map of nighttime for BCC, URB, and LSG (e–g), and probability density distribution of the separate contributions for daytime (d) and nighttime (h).

cities<sup>4</sup>. According to one projection, the total population in the megacities with more than 1 million inhabitants is projected to increase to 2.4 billion by 2030<sup>38</sup>. The LST trend in Fig. 2 suggests that these people could experience additional heat exposure around 0.30 K on top of the background warming trend. Although this temperature increment seems small, it would have a large effect on the frequency of heatwaves because the occurrence frequency of high temperatures is very sensitive to the shift of the mean<sup>39</sup>. For example, during the summer over the globe, the temperature distribution is approximately Gaussian, the frequency of hot summers with temperature exceeding a threshold of  $0.43\sigma$  is about 33%, where  $\sigma$  is the standard deviation<sup>40</sup>. By simply shifting the mean temperature of the distribution upward by only 0.30 °C, the frequency of hot summers will increase disproportionately to 55%, with the assumptions that the Gaussian distribution and the variance remain the same.

Results of our attribution analysis support the use of urban greening as an effective strategy to mitigate urban surface warming<sup>41</sup>. The greening trend reported here for most cities

appears to be unintentional (Supplementary Fig. 5), presumably associated with a longer growing season in the warmer urban environment than in the rural background<sup>42</sup>. In some cities, the greening trend is at least partly a result of active urban adaptation efforts. For example, the City of Chicago in the US has been expanding street tree coverage to reduce urban temperature since a severe heatwave in 1995<sup>43</sup>, and our trend analysis reveals that the EVI in the City of Chicago has been increasing at  $0.011 \text{ decade}^{-1}$ , a rate that is more than three times higher than the mean rate for megacities ( $0.0026 \text{ decade}^{-1}$ ; Supplementary Fig. 11). However, in the global south or equatorial regions of Africa and South America, the urban cores have experienced loss of vegetation (Supplementary Fig. 5) despite the general greening trend of the terrestrial land<sup>29</sup>. Our attribution analysis suggests that protection of urban vegetation can slow down daytime surface warming of these cities by  $0.084 \text{ K decade}^{-1}$  (Fig. 3).

Similar relations between surface UHI intensity and population have been revealed at the global scale<sup>44</sup>. We however need to note that there are large differences between this investigation and the

previous study by Manoli et al.<sup>44</sup>. Here we mainly focused on the long-term surface warming trends, while the focus of the previous study by Manoli et al.<sup>44</sup> was on the spatial variability of surface UHI. Several mitigation options are available to address the faster urban surface warming through our analysis and previous reports. Our results support that urban greening is an effective strategy to mitigate urban surface warming. The use of green space and building structure to reduce intra-city aerodynamic roughness and surface imperviousness within cities are also effective ways to mitigate urban heat<sup>41,45</sup>. The management of urban surface properties like surface albedo and emissivity modifications is also a viable alternative, because they influence heat storage and net radiation in urban areas<sup>44</sup>. Policymakers should also consider the intertwining climatic conditions experienced by citizens due to both urban surface warming and climate change rather than localized warming alone<sup>36,44</sup>.

## Methods

**Satellite datasets.** Three MODIS datasets (2002–2021) were used in this study, including the LST (MYD11A2, 8-day composites), EVI (MOD13A2, 16-day composites), and yearly land cover type (MCD12Q1) datasets. All these datasets were downloaded from the EOSDIS (<https://earthdata.nasa.gov/>). The LST dataset includes two overpasses per day (at ~01:30 am and ~13:30 pm local solar time). The spatial resolution of the LST and EVI data is 1000 m, and that for the land cover type data are 500 m. The land cover type data were resampled to 1 km to match resolution of the LST and EVI data using the nearest neighbor method.

**City cluster data.** The city cluster boundary dataset was obtained from global urban boundary (GUB) data in 2018 (<http://data.ess.tsinghua.edu.cn/>). City clusters with a size larger than 50 km<sup>2</sup> at the beginning of the study period were considered in this study. In total, 2080 city clusters were used. They were divided into four groups, labeled as small, medium, large, and megacities, according to ascending order in urban size between the 0 to 25th, 25th to 50th, 50th to 75th, and 75th to 100th percentile, respectively. The corresponding mean areas are 63, 95, 194 and 475 km<sup>2</sup>. Here we choose urban built area as a proxy of city size mainly by referring to previous studies<sup>46,47</sup>, which have examined the relations between urban warming and city size as measured by urban built area. There are 844, 132, 604, 346, 130, 24 cities in Asia, Africa, Europe, North America, South America, and Oceania, respectively. This city cluster dataset was generated from the global artificial impervious area product, and it corresponds well with the global nighttime light data and population data<sup>48</sup>. Due to the high quality, the GUB dataset have been used extensively in various similar studies<sup>49,50</sup>. This dataset was resampled to the resolution of 1 km to match those of the satellite data using the nearest neighbor method. The rural buffer of each city cluster was set to match the size of the city cluster, noting that the urban expansion information for each city cluster was obtained by the MODIS yearly land cover type dataset (i.e., MCD12Q1) rather than by this city cluster boundary dataset. For each city cluster, the pixels classified as ‘urban and built-up areas’ by MODIS land cover product were defined as urban areas. Then the urban expansion was determined by examining the identified urban area from 2002 to 2021. Note that we used the data in 2020 to represent the land cover type of 2021, because the land cover type products are only available until 2020.

**Population data.** The population dataset (2002 to 2020) was obtained from the Oak Ridge National Laboratory (<https://landscan.ornl.gov/>). This dataset was generated at a 1 km grid resolution from land cover type, nighttime light, and high-resolution panchromatic imagery<sup>51</sup>. Note that we used the 2020 data to represent the population of 2021, because the population data are only available until 2020.

**Reanalysis data.** The monthly reanalysis SAT for the period of 2002 to 2021 was provided by the Goddard Earth Sciences Data and Information Services Center (GES DISC) (<https://disc.gsfc.nasa.gov/>), produced by the common Global Land Data Assimilation System (GLDAS). The original data has a grid resolution of 9 km. It was also resampled to 1 km to match the grid size of the satellite data using the nearest neighbor method. The SAT trend for each city cluster was calculated as the mean of all the grids in the city cluster using linear regression. Before the trend calculation, all the monthly SATs within an annual cycle were averaged into yearly mean value to eliminate the seasonal effect.

**Detection of trends in urban core, rural background, and transitional land.** To avoid the confounding effect of transitional pixels on time trend detection, we divided the pixels in each cluster and in its buffer into three groups: urban core, rural background, and transitional. Delineation is made with the help of a breakpoint detection algorithm (Breaks For Additive Season and Trend, BFAST) and the annual data on LST and land cover type. The urban core pixels are those

tagged as urban by the land cover product at the beginning and the end of the observation period but exclude those that exhibit a breakpoint behavior. The rural background consists of pixels tagged as land cover types other than urban or water and excludes pixels with breakpoint behaviors. Water bodies are removed because they are not suitable as rural background for surface UHI calculations<sup>25,50</sup>. The transitional pixels are those that exhibit breakpoint behaviors during the observational period.

We used the BFAST algorithm to determine abrupt changes, or breakpoints, and time trends in both satellite LST and EVI time series<sup>52</sup>. This algorithm decomposes the time series into the trend, the seasonal, and the remainder components (refer to Supplementary Note 4):

$$S(t) = S_{tr}(t) + S_{sn}(t) + S_{re}(t) \\ = (\alpha_i(t) + \beta_j) + (A \cdot \sin(2\pi f(t - t_0) + \theta)) + T_{re}(t) \quad (1)$$

where  $S(t)$  is the observed LST/EVI at time  $t$  ( $t = 1, \dots, n$ , where  $n$  is the number of LST/EVI observations throughout the period from 2002 to 2021);  $S_{tr}(t)$ ,  $S_{sn}(t)$ , and  $S_{re}(t)$  are the trend, seasonal, and remainder components, respectively;  $\alpha_i(t)$  and  $\beta_j$  represent the segment-specific trends and intercepts on each sub-period within the time series LST/EVI data;  $A$ ,  $t_0$ , and  $\theta$  denote the seasonal amplitude, day of spring equinox and phase shift respectively; and  $f$  is the frequency, set as a constant 1/46 for LSTs and 1/23 for EVI, due to the temporal resolution of LST (8-day) and EVI (16-day) data (i.e., 46 LST observations and 23 EVI observations per year). More information on major acronyms and abbreviations can be found in Supplementary Table 5.

The BFAST algorithm was implemented with the ‘bfast’ package in R (<http://bfast.r-forge.r-project.org/>)<sup>52</sup>; and the ordinary least squares residuals-based moving sum test was applied to test whether abrupt changes appear within time series data. With the BFAST algorithm, we obtained the abrupt changes (i.e., breakpoints) and trends for each pixel of the LST and EVI data for each city cluster (refer to Supplementary Note 4). For each city cluster, the trends at the urban core and rural background were calculated based on all the available pixels within the urban core and rural background, respectively. Due to the segment-specific trends for transitional pixels, the trends in the transitional land were calculated as the mean of all the grids tagged as transitional pixels using linear regression. The 8-day interval LST were averaged into annual means to suppress the seasonal effect.

Here we chose the BFAST algorithm rather than the simple land use product to determine urban core, rural background, and transitional lands. This is mostly because the latter usually omit the land transitions, such as intra-urban renewal and redevelopment in a city center, that can distort the estimation of warming trend but are not tagged by the simple land use product<sup>53</sup>. The BFAST algorithm has been used widely by the remote sensing community to determine transitional pixels with a high accuracy<sup>52</sup>. In the present study, the percent of pixels that have undergone transitional change detected by the BFAST algorithm (20.3%) is greater than the pixels tagged as land cover change with the simple land use product (14.7%). This higher percent confirms that the BFAST algorithm is better at determining land transitions, especially for those that are not revealed in the land use product.

The surface UHI intensity was calculated as the difference in LST between the urban core and the rural background pixels. The trend in the surface UHI intensity was calculated by subtracting the trend at the urban core from that in the rural background.

**Attribution of urban surface warming.** The individual contributions from URB, BCC, and LSG to urban surface warming trends were quantified with the least square-based statistical attribution approach. This approach and its derivative version have been successfully used to isolate the contributions of urbanization and greenhouse gas emissions to the observed warming in China<sup>13</sup>. The statistical attribution approach expresses the observed urban core temperature as a linear combination of the component contributions, as:

$$T_{OBS}(t) = \beta_{BCC}(T_{BCC} - \nu_{BCC}) + \beta_{URB}(T_{URB} - \nu_{URB}) + \beta_{LSG}(T_{LSG} - \nu_{LSG}) + \varepsilon \quad (2)$$

where  $T_{OBS}$  is the yearly anomaly (the observed change of annual mean LST as referenced to that in the previous year) during the study period;  $T_{BCC}$ ,  $T_{URB}$ , and  $T_{LSG}$  are changes in temperature signals attributed to contributions from BCC, URB, and LSG, respectively;  $\beta_{BCC}$ ,  $\beta_{URB}$ , and  $\beta_{LSG}$  are the associated scaling factors;  $\nu_{BCC}$ ,  $\nu_{URB}$ , and  $\nu_{LSG}$  are, respectively, the noises from internal variability in BCC, URB and LSG components, which were included to reduce the possible uncertainties induced by the presence of noises in variables; and  $\varepsilon$  is a residual error term. Note that the annual mean  $T_{OBS}$ ,  $T_{BCC}$ ,  $T_{URB}$ , and  $T_{LSG}$  were calculated to suppress natural variability such as the seasonal effect<sup>13</sup>. The scaling factors and noise terms were estimated using the total least squares method in order to account for contributions from BCC, URB, and LSG to  $T_{OBS}$  more appropriately.

The BCC component ( $T_{BCC}$ ) was given by SAT from reanalysis data (Supplementary Fig. 12) at rural areas for each city<sup>54</sup>, for which the difference between LST and SAT trends could be reconciled by the scaling factor  $\beta_{BCC}$ . We further need to note that the reanalysis SAT data was used mainly by referring to previous studies<sup>18</sup>, which pointed out that assimilation models do not account for land use changes and therefore should not include urbanization signals<sup>2</sup>. Nevertheless, there may exist possible uncertainties induced by urbanization signals

involved in reanalysis SAT data. These urbanization signals may arise from the data assimilation of different datasets when generating reanalysis data. Therefore, the reanalysis SAT data over urban areas were entirely excluded to reduce the possible uncertainties related to the possible urbanization signals involved in reanalysis data.

The URB component ( $T_{URB}$ ) was set as the LST variations induced by urban population change through the statistical relationship between LST and population obtained at the pixel level. We quantified  $T_{URB}$  based on the widely used 'space-for-time substitution' approach<sup>55</sup>. For each city, we established the statistical relationship between yearly population density and LST anomalies (the observed change of population density or LST as referenced to those in the previous year) from 2002 to 2021 at the pixel level. Here the logarithmic function between LST and population density was used mainly due to the nonlinearity between these two parameters<sup>44</sup>. Using the mean yearly anomalies in population density at the city level as the prediction variable, the  $T_{URB}$  was estimated based on the established logarithmic function between LST and population density.

The LSG component ( $T_{LSG}$ ) indicates the LST variations induced by vegetation change over the urban core (i.e., urban greening or degreening over urban core)<sup>24</sup>. Here the surface warming due to urban greening was estimated indirectly based on the statistical relationship between EVI and LST (Supplementary Fig. 13). Such a relationship was obtained over rural background where the surface is less impacted by urbanization when compared with urban core. The included scaling factor  $\beta_{LSG}$  can also help adjust the differences in the LST-LSG relationships between rural background and urban core. We are also aware that this representation is not flawless because of the existence of possible oscillations<sup>24</sup>.

### Data availability

The MODIS data are publicly available at <https://e4ftl01.cr.usgs.gov/>; the city cluster boundary dataset is publicly available at <http://data.ess.tsinghua.edu.cn/>; the population dataset is publicly available at <https://landscan.ornl.gov/>; and the reanalysis data are publicly available at <https://disc.gsfc.nasa.gov/>. The major code and data generated from the original datasets as described in the article as well as supplementary materials are also available at <https://zenodo.org/record/6568484>.

### Code availability

The breakpoint detection algorithm (Breaks For Additive Season and Trend, BFAST) used in this study is available as software modules in R<sup>52</sup>.

Received: 2 January 2022; Accepted: 23 August 2022;

Published online: 29 September 2022

### References

- Hsu, A., Sheriff, G., Chakraborty, T. & Many, D. Disproportionate exposure to urban heat island intensity across major US cities. *Nat. Commun.* **12**, 2721 (2021).
- Zhao, L. et al. Global multi-model projections of local urban climates. *Nat. Clim. Chang.* **11**, 152–157 (2021).
- Oke, T. R. The energetic basis of the urban heat island. *Q. J. Roy. Meteor. Soc.* **108**, 1–24 (1982).
- Li, X. et al. Global urban growth between 1870 and 2100 from integrated high resolution mapped data and urban dynamic modeling. *Commun. Earth Environ.* **2**, 1–10 (2021).
- Pachauri, R. K. et al. Climate change 2014: Synthesis report. Contribution of Working Groups I, II and III to the fifth assessment report of the Intergovernmental Panel on Climate Change / R. Pachauri and L. Meyer (editors), Geneva, Switzerland, IPCC, 151 p., ISBN: 978-92-9169-143-2. (2014).
- Mora, C. et al. Global risk of deadly heat. *Nat. Clim. Chang.* **7**, 501–506 (2017).
- Dunne, J. P., Stouffer, R. J. & John, J. G. Reductions in labour capacity from heat stress under climate warming. *Nat. Clim. Chang.* **3**, 563–566 (2013).
- Anderson, G. B. & Bell, M. L. Heat waves in the United States: mortality risk during heat waves and effect modification by heat wave characteristics in 43 US communities. *Environ. Health Persp.* **119**, 210–218 (2011).
- Oleson, K. W. et al. Interactions between urbanization, heat stress, and climate change. *Clim. Chang.* **129**, 525–541 (2015).
- Ballester, J., Robine, J., Herrmann, F. & Rodo, X. Long-term projections and acclimatization scenarios of temperature-related mortality in Europe. *Nat. Commun.* **2**, 1–8 (2011).
- Estrada, F. & Perron, P. Disentangling the trend in the warming of urban areas into global and local factors. *Ann. N. Y. Acad. Sci.* **1504**, 230–246 (2011).
- Jones, P. D., Lister, D. & Li, Q. Urbanization effects in large-scale temperature records, with an emphasis on China. *J. Geophys. Res. Atmos.* **113**, D16122 (2008).
- Sun, Y. et al. Contribution of urbanization to warming in China. *Nat. Clim. Chang.* **6**, 706–709 (2016).
- Ren, G. et al. Urbanization effects on observed surface air temperature trends in North China. *J. Clim.* **21**, 1333–1348 (2008).
- Yang, X., Hou, Y. & Chen, B. Observed surface warming induced by urbanization in east China. *J. Geophys. Res.* **116**, D14113 (2011).
- Zhou, L. et al. Evidence for a significant urbanization effect on climate in China. *Proc. Natl. Acad. Sci. USA* **101**, 9540–9544 (2004).
- Hansen, J. et al. A closer look at United States and global surface temperature change. *J. Geophys. Res. Atmos.* **106**, 23947–23963 (2001).
- Kalnay, E. & Cai, M. Impact of urbanization and land-use change on climate. *Nature* **423**, 528–531 (2003).
- Fujibe, F. Urban warming in Japanese cities and its relation to climate change monitoring. *Int. J. Climatol.* **31**, 162–173 (2011).
- Kataoka, K., Matsumoto, F., Ichinose, T. & Taniguchi, M. Urban warming trends in several large Asian cities over the last 100 years. *Sci. Total Environ.* **407**, 3112–3119 (2009).
- Ajaaj, A. A., Mishra, A. K. & Khan, A. A. Urban and peri-urban precipitation and air temperature trends in mega cities of the world using multiple trend analysis methods. *Theor. Appl. Climatol.* **132**, 403–418 (2018).
- Varquez, A. C. G. & Kanda, M. Global urban climatology: a meta-analysis of air temperature trends (1960–2009). *NPJ Clim. Atmos.* **1**, 1–8 (2018).
- Stewart, I. D. & Oke, T. R. Local climate zones for urban temperature studies. *Bull. Am. Meteorol. Soc.* **93**, 1879–1900 (2012).
- Yao, R. et al. Greening in rural areas increases the surface urban heat island intensity. *Geophys. Res. Lett.* **46**, 2204–2212 (2019).
- Chakraborty, T. & Lee, X. A simplified urban-extent algorithm to characterize surface urban heat islands on a global scale and examine vegetation control on their spatiotemporal variability. *Int. J. Appl. Earth Obs. Geoinf.* **74**, 269–280 (2019).
- Dousset, B. et al. Satellite monitoring of summer heat waves in the Paris metropolitan area. *Int. J. Climatol.* **31**, 313–323 (2011).
- Zhang, Y. et al. Reanalysis of global terrestrial vegetation trends from MODIS products: browning or greening? *Remote Sens. Environ.* **191**, 145–155 (2017).
- Richards, D. R. & Belcher, R. N. Global changes in urban vegetation cover. *Remote Sens.* **12**, 23 (2019).
- Zhu, Z. et al. Greening of the earth and its drivers. *Nat. Clim. Chang.* **6**, 791–795 (2016).
- Piao, S. et al. Characteristics, drivers and feedbacks of global greening. *Nat. Rev. Earth Environ.* **1**, 14–27 (2020).
- Wohlfahrt, G., Tomelleri, E. & Hammerle, A. The urban imprint on plant phenology. *Nat. Ecol. Evol.* **3**, 1668–1674 (2019).
- Chen, C. et al. China and India lead in greening of the world through land-use management. *Nat. Sustain.* **2**, 122–129 (2019).
- Zhu, Z. et al. Including land cover change in analysis of greening trends using all available Landsat 5, 7, and 8 images: a case study from Guangzhou, China (2000–2014). *Remote Sens. Environ.* **185**, 243–257 (2016).
- Lee, X. et al. Observed increase in local cooling effect of deforestation at higher latitudes. *Nature* **479**, 384–387 (2011).
- Oke, T. R., Mills, G., Christen, A. & Voogt, J. A. Urban climate. (Cambridge University Press, 2017).
- Estrada, F., Botzen, W. J. W. & Tol, R. S. J. A global economic assessment of city policies to reduce climate change impacts. *Nat. Clim. Chang.* **7**, 403–406 (2017).
- Imhoff, M. L., Zhang, P., Wolfe, R. E. & Bounoua, L. Remote sensing of the urban heat island effect across biomes in the continental USA. *Remote Sens. Environ.* **114**, 504–513 (2010).
- United Nations. Department of Economic and Social Affairs, Population Division. The World's Cities in 2018—Data Booklet (ST/ESA/SER.A/417). (2018).
- Houghton, J. Global Warming: The Complete Briefing. Cambridge University Press: the fifth Edition (2015).
- Hansen, J., Sato, M. & Ruedy, R. Perception of climate change. *Proc. Natl. Acad. Sci. USA* **109**, 14726–14727 (2012).
- Li, D. et al. Urban heat island: Aerodynamics or imperviousness? *Sci. Adv.* **5**, eaau4299 (2019).
- Li, D. et al. The effect of urbanization on plant phenology depends on regional temperature. *Nat. Ecol. Evol.* **3**, 1661–1667 (2019).
- Mackey, C. W., Lee, X. & Smith, R. B. Remotely sensing the cooling effects of city scale efforts to reduce urban heat island. *Build. Environ.* **49**, 348–358 (2012).
- Manoli, G. et al. Magnitude of urban heat islands largely explained by climate and population. *Nature* **573**, 55–60 (2019).
- Zhao, L., Lee, X., Smith, R. B. & Oleson, K. Strong contributions of local background climate to urban heat islands. *Nature* **511**, 216–219 (2014).
- He, Y., Jia, G., Hu, Y. & Zhou, Z. Detecting urban warming signals in climate records. *Adv. Atmos. Sci.* **30**, 1143–1153 (2013).
- Zhou, B., Rybski, D. & Kropp, J. P. The role of city size and urban form in the surface urban heat island. *Sci. Rep.* **7**, 1–9 (2017).



48. Li, X. et al. Mapping global urban boundaries from the global artificial impervious area (GAIA) data. *Environ. Res. Lett.* **15**, 094044 (2020).
49. Chen, B. et al. Mapping essential urban land use categories with open big data: results for five metropolitan areas in the United States of America. *ISPRS J. Photogramm. Remote Sens.* **178**, 203–218 (2021).
50. Liu, Z. et al. Taxonomy of seasonal and diurnal clear-sky climatology of surface urban heat island dynamics across global cities. *ISPRS J. Photogramm. Remote Sens.* **187**, 14–33 (2022).
51. Dobson, J. E. et al. Landsat: a global population database for estimating populations at risk. *Photogramm. Eng. Remote Sens.* **66**, 849–857 (2000).
52. Verbesselt, J., Hyndman, R. J., Newnham, G. & Culvenor, D. S. Detecting trend and seasonal changes in satellite image time series. *Remote Sens. Environ.* **114**, 106–115 (2010).
53. Hentze, K., Thonfeld, F. & Menz, G. Beyond trend analysis: how a modified breakpoint analysis enhances knowledge of agricultural production after Zimbabwe's fast track land reform. *Int. J. Appl. Earth Obs. Geoinf.* **62**, 78–87 (2017).
54. Krayenhoff, E. S. et al. Diurnal interaction between urban expansion, climate change and adaptation in US cities. *Nat. Clim. Chang.* **8**, 1097–1103 (2018).
55. Pickett, S. T. A. Space-for-time substitution as an alternative to long-term studies. In: *Long-term studies in ecology*. Springer (1989).

### Acknowledgements

This research is jointly supported by the National Key Research and Development Programs for Global Change and Adaptation (2017YFA0603604), the National Natural Science Foundation of China (42171306), and the Jiangsu Provincial Natural Science Foundation (BK20180009). We are also very grateful for the financial support from the National Youth Talent Support Program of China. The Pacific Northwest National Laboratory (PNNL) is operated for DOE by Battelle Memorial Institute under contract DE-AC05-76RL01830.

### Author contributions

W.Z. and X.L. designed the research, Z.L. performed the data analysis; Z.L., W.Z., and X.L. wrote the manuscript; and B.B., J.V., J.L., T.C., Z.W., M.L., and F.H. contributed ideas to the data analysis, interpretation of results, or manuscript revision.

### Competing interests

The authors declare no competing interests.

### Additional information

**Supplementary information** The online version contains supplementary material available at <https://doi.org/10.1038/s43247-022-00539-x>.

**Correspondence** and requests for materials should be addressed to Wenfeng Zhan, Manchun Li or Xuhui Lee.

**Peer review information** *Communications Earth & Environment* thanks Francisco Estrada, Munir Nayak, and the other, anonymous, reviewer(s) for their contribution to the peer review of this work. Primary Handling Editors: Clare Davis and Heike Langenberg.

**Reprints and permission information** is available at <http://www.nature.com/reprints>

**Publisher's note** Springer Nature remains neutral with regard to jurisdictional claims in published maps and institutional affiliations.



**Open Access** This article is licensed under a Creative Commons Attribution 4.0 International License, which permits use, sharing, adaptation, distribution and reproduction in any medium or format, as long as you give appropriate credit to the original author(s) and the source, provide a link to the Creative Commons license, and indicate if changes were made. The images or other third party material in this article are included in the article's Creative Commons license, unless indicated otherwise in a credit line to the material. If material is not included in the article's Creative Commons license and your intended use is not permitted by statutory regulation or exceeds the permitted use, you will need to obtain permission directly from the copyright holder. To view a copy of this license, visit <http://creativecommons.org/licenses/by/4.0/>.

© The Author(s) 2022